OPTICA

High-coherence hybrid-integrated 780 nm source by self-injection-locked second-harmonic generation in a high-Q silicon-nitride resonator

Bohan Li,[1],[†] Zhiquan Yuan,[1],[†] Warren Jin,[2],[†] Lue Wu,[1] Joel Guo,[3] Qing-Xin Ji,[1] Avi Feshali,[2] Mario Paniccia,[2] John E. Bowers,[3] and Kerry J. Vahala[1],*

[1]*T. J. Watson Laboratory of Applied Physics, California Institute of Technology, Pasadena, California 91125, USA*
[2]*Anello Photonics, Santa Clara, California 95054, USA*
[3]*ECE Department, University of California Santa Barbara, Santa Barbara, California 93106, USA*
[†]*These authors contributed equally to this paper.*
*vahala@caltech.edu

Visible, high-coherence optical sources are important to a wide range of applications spanning spectroscopy to precision timing. Integration of these sources on a semiconductor chip is a necessary step if the systems that use these devices are to be made compact, portable, and low power. Here, by self-injection-locking a 1560 nm distributed feedback semiconductor laser to a high-Q silicon-nitride resonator, a high-coherence 780 nm second-harmonic signal is generated via the photogalvanic-induced second-order nonlinearity. A record-low frequency noise floor of 4 Hz^2/Hz is achieved for the 780 nm emission. The approach can potentially generate signals over a wide range of visible and near-visible bands, and thereby help transition many table-top systems into a fieldable form. © 2023 Optica Publishing Group under the terms of the [Optica Open Access Publishing Agreement](#)

Highly coherent visible laser sources play a crucial role in the operation of optical atomic clocks [1], automotive LiDAR [2], and sensing systems [3]. However, existing bench-top visible lasers are both costly and bulky, limiting their use beyond laboratory environments including application in future navigation and sensing systems. To address this challenge, we generate visible light in a high-Q silicon nitride microcavity that is hybridly integrated to a semiconductor laser operating in the near-infrared band. The cavity both line narrows the laser through self-injection-locking (SIL) [4,5] and generates the high-coherence visible signal as a second-harmonic (SH) signal by way of the photogalvanic field-induced second-order nonlinearity [6] and the all-optical-poling effect [7–9] in Si$_3$N$_4$. Frequency noise is reduced by 100-fold compared with previous integrated visible lasers [10–13]. The approach can be readily tuned to any visible or near-visible band.

The resonator is fabricated using the ultra-low-loss silicon-nitride photonic platform [4,14] with a 100 nm thick silicon-nitride waveguide core and a 2.2 μm thick silica top cladding. The resonator has a 5 μm waveguide width and a 850 μm radius. The free-spectral range is 35.52 GHz at 1560 nm. Two pulley couplers are designed for coupling at both the near-infrared and visible bands. The near-infrared coupler has a 2.3 μm waveguide width with a 3.5 μm gap that is designed to prevent coupling to the visible mode. The visible coupler has a 1.6 μm waveguide width with a 0.3 μm gap that is designed to reduce coupling to the near-infrared mode.

The resonator is first characterized using the experimental setup shown in Fig. 1(a). A four-channel fiber array and a lensed fiber are used to couple to near-infrared and visible resonances simultaneously. To probe the resonances, the output of a near-infrared tunable laser is split with one output doubled in frequency using a periodically poled lithium niobate (PPLN) crystal. In this way, first- and SH probe waves are generated to characterize resonator spectra in these bands. Because the photogalvanic effect induces optical poling to thereby establish the quasi-phase-matching condition [9], a visible mode having twice the pumping frequency will achieve SH generation regardless of its propagation constant. To establish this condition, the Si$_3$N$_4$ chip is temperature controlled to tune the mode spectra. Tuning over no more than one free-spectral range is sufficient, and in the current setup, a chip temperature of 45°C aligns the pump resonance at 1560.1 nm with a visible resonance at 780.05 nm. Photogalvanic-induced SH generation can be readily observed when scanning the pump laser across the near-infrared resonance, as shown in Fig. 1(b). Continuous-wave SH power measurements with the pump laser frequency fixed at the cavity resonance are shown in the inset of Fig. 1(b). The SH conversion efficiency is estimated to be 114 ± 31%W (average over measured powers), and SH output power as high as 24 mW is measured (in the bus waveguide). The total Q factors (Q_t) of the pump and SH modes are determined by transmission spectra measurements shown in Figs. 1(c) and 1(d).

To achieve a high-coherence visible light source in a compact foot print, we replace the bulk tunable laser with a distributed feedback (DFB) chip laser as shown in the experimental setup in Figs. 1(e) and 1(f). The DFB laser is endfire-coupled to the silicon-nitride chip and can deliver 20 mW pump power to the resonator waveguide (accounting for 6 dB facet coupling loss). Backscatter-induced feedback from the resonator to the laser provides SIL that
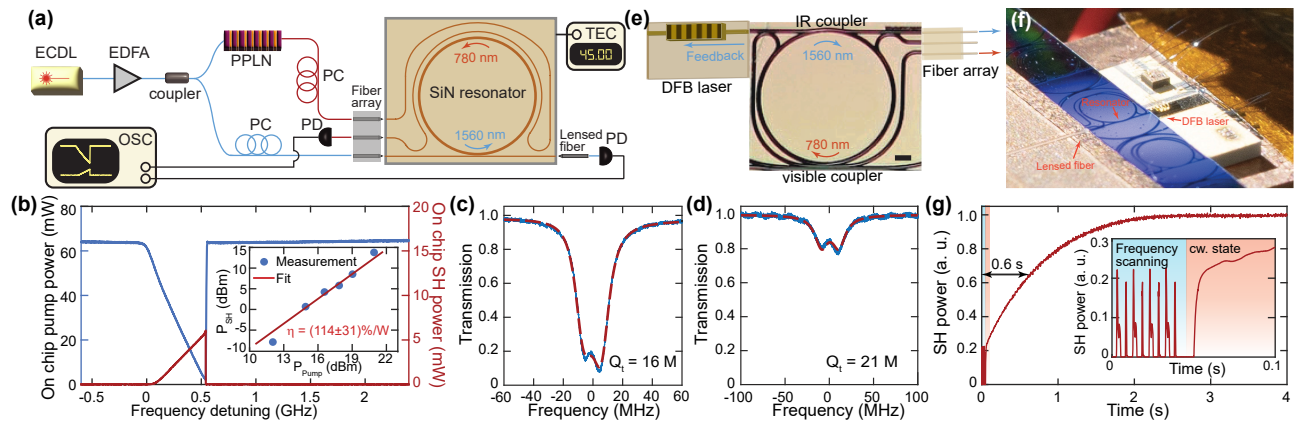
Fig. 1. Experimental setups and characterization of the Si$_3$N$_4$ resonator and SH generation performance. (a) Experimental setup used to determine the phase matching condition and characterize the SH performance of the Si$_3$N$_4$ resonator. ECDL, external cavity diode lasers; EDFA, erbium-doped fiber amplifier; PPLN, periodically poled lithium niobate; PC, polarization controller; PD, photodetector; OSC, oscilloscope; TEC, thermoelectric cooler. (b) Measured on-chip transmission pump power (left axis) and generated SH power (right axis) when scanning the frequency of the pump laser across a cavity resonance at the phase matching condition. Inset: measured on-chip SH power (blue dots) plotted versus pump power levels. The frequency conversion efficiency is fit by the red line with a slope of two. Within our measurement range, the SHG efficiency (η in %/W) is found to be constant. (c) Transmission spectrum of the pump resonance at 1560.1 nm. (d) Transmission spectrum of the SH resonance at 780.05 nm. In (c), (d), the experimental measurements are plotted in blue, and the theoretical fittings are plotted in red. Each resonance exhibits backscatter-induced splitting, and total Q factors (Q_t) are indicated. The leakage of 1560 nm light into the 780 nm pulley coupler and the multimode nature of the 780 nm waveguide make determination of the intrinsic (i.e., ring-only) Q factors of the 1560 and 780 nm modes difficult (see Appendix A). (e) Schematic of the hybrid-integrated frequency conversion laser, where a DFB laser is endfire-coupled to a high-Q silicon-nitride microresonator to provide feedback to the laser. The upper and lower waveguides are designed for coupling at 1560 nm and 780 nm, respectively. The scale bar is 200 μm. (f) Photograph of the hybrid-integrated frequency conversion laser in (e). (g) Time response of the SH power after the DFB laser frequency is stopped at the operation point. Inset: zoom-in of the main plot. Prior to fixing the DFB laser frequency, the pump laser frequency is scanned, and SH power changes periodically during frequency scanning (blue region). When the scanning is stopped, SH power builds to steady state (red region).

dramatically reduces the laser frequency noise [4,5]. Upon current tuning the DFB laser frequency into the 1560.1 nm resonance, the optical poling process is initialized through the field-induced photogalvanic effect. This process is monitored by scanning the frequency of the DFB laser around the resonance by modulating the pump current with a function generator. The SH signal produced during forward and backward scanning is shown in the inset of Fig. 1(g) (blue region). The function generator is then turned off, and the DFB frequency self-injection-locks into the resonance. The resulting SH signal time evolution is shown over a short time interval in the inset of Fig. 1(g) (red region) and over several seconds in the main panel. The SH power build-up features a 0.6 s rise time and takes only a few seconds to reach steady state. In steady-state operation, the SH power at 780 nm reaches over 0.5 mW on-chip as monitored via a lensed fiber (12 dB coupling loss).

The SIL 1560 nm light and SH generated 780 nm light are then further analyzed to determine their frequency noise performance [Fig. 2(a)]. The SH signal is sent to a delayed self-homodyne detection setup with quadrature-point locking [15], and its measured frequency noise is shown as the red trace in Fig. 2(b). The peak at 18 kHz offset in the spectrum is due to the feedback loop response of a fiber stretcher used to maintain the quadrature point. At high offset frequencies, the photodetector (PD) white noise is suppressed using a cross-correlation technique [16,17], and the SH signal achieves 4 Hz^2/Hz noise floor above 6 MHz offset frequency, corresponding to a record-low 25 Hz instantaneous linewidth for visible on-chip sources. The frequency noise of the self-injection locked pump laser is characterized with a self-heterodyne approach [17], and the result is shown as the blue curve in Fig. 2(b). Compared with the free-running DFB

laser noise (gray trace), the SIL process suppresses the noise by 40 (32) dB at 100 kHz (1 MHz) offset frequency. The generated SH laser noise is four times higher than the SIL pump laser noise due to coherent photon conversion [12]. Specifically, the phase fluctuation of the pump field is doubled in the SH signal through the squaring of the pumping field. The corresponding SH spectral density function therefore experiences a factor of four increase (6 dB) relative to the pump. The difference in these spectra at high offset frequencies is due to pump laser spontaneous emission noise in the 1560 nm signal, and the measurement of this signal at the transmission port of the coupled resonator system.

High intra-cavity photon density and resonant backscattering make this system prone to Kerr frequency comb generation [4]. SIL comb formation is governed by feedback phase and frequency detuning [18,19], and these parameters also provide a way to favor single-mode lasing over comb generation. In the present device the laser-to-chip gap (feedback phase) and pump current (frequency detuning) provide useful controls. The latter is illustrated in Fig. 3(a) where the transmitted pumping power and the SH power are plotted versus DFB laser current scan. Distinct regimes where the single-frequency SIL state and the comb state appear are indicated. In the comb state, only the pump comb line can be frequency doubled due to the phase matching condition. The operation point used in the previous power and noise measurements is indicated. Typical SH spectra in the two regimes are shown in Figs. 3(b) and 3(c). Reduced SH power is apparent for the comb state since intracavity pump power is reduced by comb formation.

In conclusion, we have demonstrated a record-low 4 Hz^2/Hz frequency noise floor for a hybrid-integrated visible light source
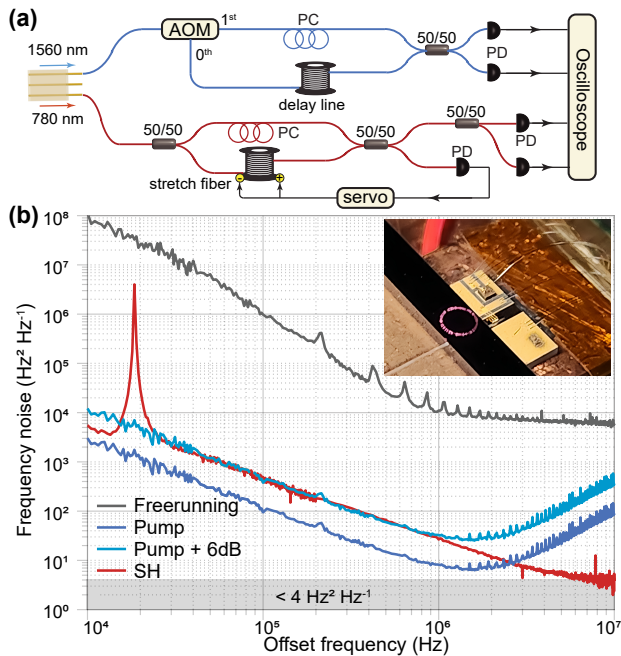
Fig. 2. Frequency noise measurement for SIL pump laser and generated SH laser. (a) Frequency noise measurement setups for both the SIL 1560 nm laser and the SH 780 nm laser. AOM, acousto-optic modulator. (b) Measured single-sideband frequency noise spectrum. Gray, blue, and red traces show the frequency noise spectra of the free-running DFB signal, SIL pump signal (1560 nm), and SH signal (780 nm), respectively. The light blue trace shows the SIL pump laser frequency noise up-shifted by 6 dB. The inset is a photograph of the device under operation with 780 nm emission visible on the ring resonator.
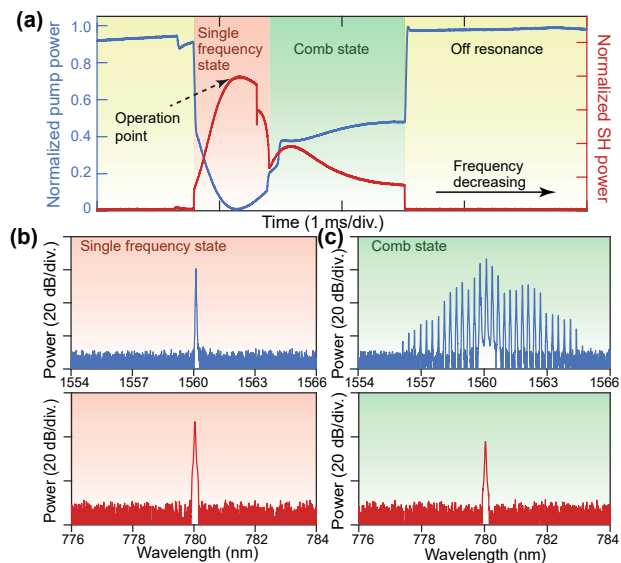

Fig. 3. Self-injection-locked laser response with pump-current-induced frequency tuning. (a) Measured SIL pump power (blue) and second-harmonic power (red) when the pump current is scanned across the resonance. When the DFB laser frequency is tuned into the cavity resonance, the near-infrared laser is initially in a single-frequency state and eventually tunes to a comb state. (b), (c) Upper panels: measured optical spectra of the near-infrared laser in the single-frequency state (b) and comb state (c). Lower panels: corresponding SH 780 nm spectra.
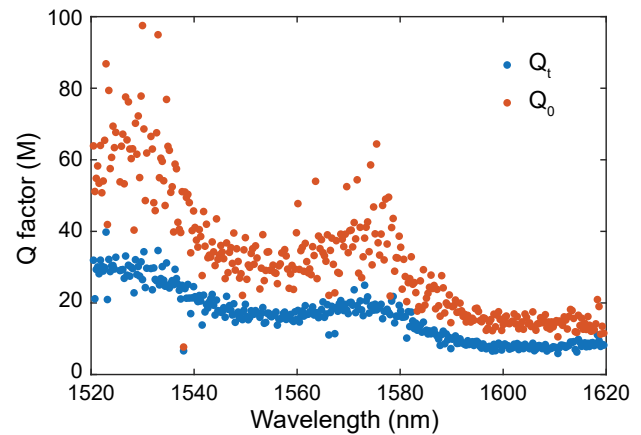

Fig. 4. Resonator total (Q_t) and intrinsic (Q_0) Q factor measurements plotted versus wavelength. The spectral peaks in measured intrinsic Q factors are believed to originate from the wavelength-dependent coupling of 1560 nm light to the 780 nm pulley coupler.

by SIL operation of a DFB laser with a high-Q Si$_3$N$_4$ resonator. The III-IV laser and the silicon-nitride resonator can be heterogeneously integrated using the integration technique described in Ref. [20]. The current resonator intrinsic Q factor is not optimal, and based on prior work could exceed 250M at 1560 nm [4]. This should further reduce frequency noise levels since the SIL noise reduction scales as Q^2 [21]. This scaling makes generation of highly coherent signals easier in the near-infrared where optical Q factors are overall much higher. The SH-SIL process therefore extends this advantage into the visible bands. Finally, the photogalvanic effect makes access to other wavelengths straightforward. Devices require only waveguide couplers designed for efficient visible and near-infrared operation.

During preparation of this paper, two other papers were reported: one on direct generation of high-coherence visible light [22] and one on SIL-SH using the photogalvanic effect [23].

APPENDIX A: COUPLER DESIGN PRINCIPLE

The 1560 nm pulley coupler waveguide width is chosen to achieve phase matching to the ring resonator fundamental eigenmode. The coupler occupies an effective arc length of about 0.1 radian of the resonator with a 3.5 µm minimum gap. This gap is too large to achieve significant interaction with the 780 nm eigenmode, thereby reducing parasitic coupling of the 780 nm mode to the 1560 nm coupler.

The 1.6 µm width of the 780 nm pulley coupler waveguide is approximately phase matched to the TE10 higher-order mode of the resonator. This substantially phase mismatches the coupler to the fundamental resonator eigenmode at 1560 nm, thereby suppressing parasitic coupling of the 1560 nm mode. The coupler gap is narrow (minimum 0.3 µm), and to further minimize perturbation to the 1560 nm mode, the gap is adiabatically reduced using the arc of an archimedian spiral. This, however, results in a coupler arc-length exceeding 1 radian, so that 780 nm optical power might undergo several coupling oscillations over the length of the coupler.

Some parasitic coupling of the 1560 nm light to the 780 nm coupler is expected. This parasitic loss channel contributes to the intrinsic Q factor of the resonator at 1560 nm, and spectral

measurements of Q factors around 1560 nm reveal an oscillatory dependence (see Fig. 4) that is believed to result from this dependence.

Disclosures.   The authors declare no conflicts of interest.

Data availability.   Data are available upon reasonable request.

REFERENCES

1. A. D. Ludlow, M. M. Boyd, J. Ye, *et al.*, Rev. Mod. Phys. **87**, 637 (2015).
2. J. Hecht, Opt. Photonics News **29**(1), 26 (2018).
3. C. L. Degen, F. Reinhard, and P. Cappellaro, Rev. Mod. Phys. **89**, 035002 (2017).
4. W. Jin, Q.-F. Yang, L. Chang, *et al.*, Nat. Photonics **15**, 346 (2021).
5. B. Li, W. Jin, L. Wu, *et al.*, Opt. Lett. **46**, 5201 (2021).
6. X. Lu, G. Moille, A. Rao, *et al.*, Nat. Photonics **15**, 131 (2021).
7. A. Billat, D. Grassani, M. H. Pfeiffer, *et al.*, Nat. Commun. **8**, 1016 (2017).
8. D. D. Hickstein, D. R. Carlson, H. Mundoor, *et al.*, Nat. Photonics **13**, 494 (2019).
9. E. Nitiss, J. Hu, A. Stroganov, *et al.*, Nat. Photonics **16**, 134 (2022).
10. A. Siddharth, T. Wunderer, G. Lihachev, *et al.*, APL Photonics **7**, 046108 (2022).
11. M. Corato-Zanarella, A. Gil-Molina, X. Ji, *et al.*, Nat. Photonics **17**, 157 (2023).
12. J. Ling, J. Staffa, H. Wang, *et al.*, Laser Photonics Rev. **17**, 2200663 (2023).
13. C. A. Franken, A. van Rees, L. V. Winkler, *et al.*, Opt. Lett. **46**, 4904 (2021).
14. M. Puckett, K. Liu, N. Chauhan, *et al.*, Nat. Commun. **12**, 934 (2021).
15. H. Lee, T. Chen, J. Li, *et al.*, Nat. Photonics **6**, 369 (2012).
16. W. F. Walls, in *Proceedings of the 1992 IEEE Frequency Control Symposium* (IEEE, 1992), pp. 257–261.
17. Z. Yuan, H. Wang, P. Liu, *et al.*, Opt. Express **30**, 25147 (2022).
18. B. Shen, L. Chang, J. Liu, *et al.*, Nature **582**, 365 (2020).
19. G. Lihachev, W. Weng, J. Liu, *et al.*, Nat. Commun. **13**, 1771 (2022).
20. C. Xiang, W. Jin, O. Terra, *et al.*, Nature **620**, 78 (2023).
21. N. Kondratiev, V. Lobanov, A. Cherenkov, *et al.*, Opt. Express **25**, 28167 (2017).
22. Z. Zhang, B. Shen, M. A. Tran, *et al.*, Optica **10**, 752 (2023).
23. M. Clementi, E. Nitiss, E. Durán-Valdeiglesias, *et al.*, in *CLEO: Science and Innovations* (Optical Society of America, 2023), paper STh4O-1.